

Rayleigh-Sommerfeld modelling with AVO

Joanna K. Cooper, Gary F. Margrave, and John Maweu

ABSTRACT

Using ray tracing to compute angles of incidence at each reflecting interface, angle-dependent reflection coefficients were introduced into the 3D Rayleigh-Sommerfeld modelling method. Previously, the method, which is based on phase-shifting of the wavefield, was limited to laterally varying, but angle-independent reflection coefficients. This advancement allows for the inclusion of realistic amplitude variation with offset (AVO) effects in model data produced by the Rayleigh-Sommerfeld method. An example in a constant velocity medium demonstrates that the modelled amplitudes closely match the expected AVO curves. The method was then applied to generating shot records over a channel model. Inspection of the shot records and subsequent migrations demonstrate the success of the method in simulating AVO effects in a complex stratigraphic setting.

INTRODUCTION

The Rayleigh-Sommerfeld method for 3D seismic modelling provides an alternative to better-known modelling techniques such as finite-difference or Kirchhoff. Often our objective in modelling in stratigraphic settings is to produce a high-frequency seismic response that includes diffraction effects. In such a case, finite-difference modelling may be computationally too expensive to produce the high frequencies. Also, we may not require the level of wavefield completeness that finite-difference modelling produces. Kirchhoff modelling is a viable alternative; however, Rayleigh-Sommerfeld modelling, which can be shown to be closely related to the Kirchhoff method, is more efficient because it operates in the frequency-wavenumber domain. The $O(N \log N)$ computing time of Rayleigh-Sommerfeld compared to $O(N^2)$ of Kirchhoff is especially attractive when large 3D models are of interest.

In 2007 we reported on the implementation of Rayleigh-Sommerfeld modelling in MATLAB (Margrave and Cooper, 2007). We demonstrated that the method produces high-fidelity models suitable for migration testing. However, a drawback of the implementation that limited its use in modelling stratigraphically complex areas was that it could not incorporate offset-dependent amplitude effects, other than simple geometric spreading. Here we describe our extension of the method to include AVO (Amplitude Variation with Offset) effects. First we recap the theory behind the Rayleigh-Sommerfeld method, which we describe as running phase-shift migration in reverse. Then we describe how AVO effects are incorporated. We then show modelled shot records produced in a constant velocity setting to confirm the accuracy of the method. Finally we show the method applied to a complex stratigraphic model.

RAYLEIGH-SOMMERFELD MODELLING

Margrave and Cooper (2007) describe the Rayleigh-Sommerfeld method following Ersoy (2007). Only a brief recap will be given here. The Rayleigh-Sommerfeld theory of diffraction (e.g. Ersoy, 2007) was proposed as a Fourier domain alternative to

Kirchhoff's theory. Today it provides the basis for phase-shift migration methods, or it can provide a modelling method as we show here. This is not new to exploration seismology (e.g. Berkhout, 1993, Gazdag, 1981) but is often overlooked in favour of more costly methods. Figure 1 shows the Rayleigh-Sommerfeld method for a single reflector. In essence, a source function is Fourier transformed over the lateral spatial coordinates, phase-shift extrapolated to the reflector, and inverse Fourier transformed. This gives the source wavefield as it is incident on the reflector. We then multiply by the "reflectivity function" of the reflector, and repeat the phase-shift operation to extrapolate the reflected wavefield back up to the receivers. Following the first-order Born approximation, the wavefield extrapolation is governed by a smooth background velocity function, and the reflectivity is decoupled from the background. At present our implementation of the Rayleigh-Sommerfeld method is limited to background media without lateral velocity gradients. This limitation is not intrinsic to the method but overcoming it will bear a computational burden.

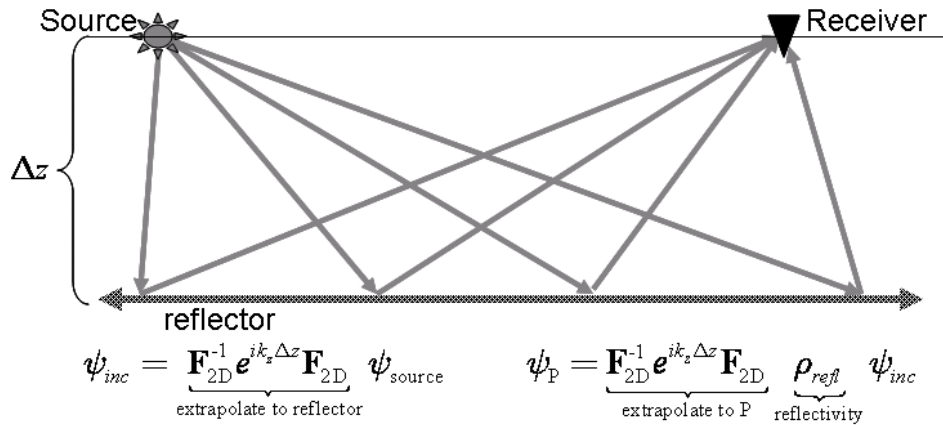


FIG. 1. The Rayleigh-Sommerfeld modelling method for a single reflector. The source wavefield is extrapolated down to the reflector, multiplied by the reflectivity, and then extrapolated back up to the receiver.

Figure 2 illustrates the process of multiplying the propagated down-going wavefield by the reflectivity function. The left panel shows a time slice through the down-going extrapolated source wavefield for a source point in the upper left corner. The middle panel shows the same slice but after multiplication by the reflectivity function. It is apparent that the reflection coefficient was everywhere negative at the incidence locations but was also much stronger in a few locales (the model is actually that shown in Figure 6). The right panel shows a time slice of the wavefield, at twice the time of the first two slices, after propagation back to the surface. After multiplication, the amplitude variations along the wavefront in the middle panel act as Huygen's sources, each producing diffractions. The recorded wavefield displays circular diffraction patterns with centres at these Huygen's sources. The reflection occurs at roughly half the offset of the final wavefront at the surface. The recorded wavefield also contains the result of similar diffractions occurring at all spatial positions that are illuminated by the down-going wavefield and arriving at various times.

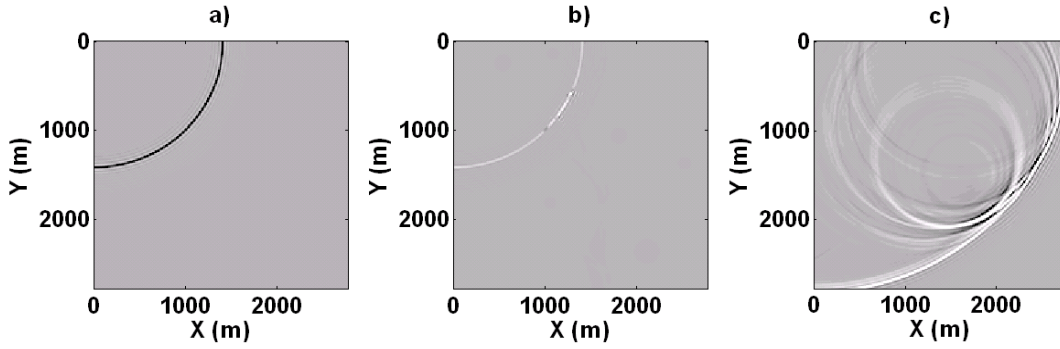


FIG. 2. Illustration of the multiplication of an extrapolated source wavefield by a reflectivity function, followed by extrapolation to receivers, intrinsic to the Rayleigh-Sommerfeld modelling method. a) Time slice through down-going wavefield at a reflector. b) Same time slice after multiplication by the reflectivity function corresponding to that depth. c) Time slice through surface-recorded wavefield at twice the traveltime of the first two slices.

In our previous paper (Margrave and Cooper, 2007), the reflectivity function of the reflector was allowed to vary arbitrarily spatially but had no dependence on the incidence angle of the source wavefield. This meant that we had to assume a single reflection coefficient for all angles and so could model near-normal incidence but not highly oblique effects such as AVO. The extension to a reflectivity function that varies spatially and also depends upon incidence angle is complicated because the Rayleigh-Sommerfeld method gives the incident wavefield as a function of space but gives no angle information. If we Fourier transform the wavefield to obtain angle information, then we lose localization in space. One way to proceed, which we intend to investigate in the coming year, is to replace the inverse Fourier transform at the reflector with an inverse Gabor transform. However, in the present investigation, we have taken a simpler approach and used ray tracing to estimate the incidence angles. This has allowed us to demonstrate that, in principle, broad-band frequency modelling that includes AVO and diffraction effects can be accomplished with the Rayleigh-Sommerfeld method.

INCLUSION OF AVO EFFECTS

Extending the Rayleigh-Sommerfeld modelling method to include angle- or offset-dependent reflection coefficients was accomplished by adding a ray-tracing step to the modelling of each shot. Rays are traced through the background velocity structure defined for the overburden, from the source position to all possible points on the reflector. The ray parameter for each ray and the corresponding point on the reflector are tabulated. As discussed above, the reflectivity function, ρ_{refl} , was previously only a function of x and y ; now ρ_{refl} may be a function of x and y and the incidence angle. In our implementation, the angle-dependent reflectivity function at any x and y position is calculated using the Aki-Richards approximation (Aki and Richards, 1980), which is defined as

$$R_{pp} = \frac{\Delta\rho}{\rho} \frac{(1-4p^2\beta^2)}{2} + \frac{\Delta\alpha}{\alpha} \frac{1}{2\cos^2 i} + \frac{\Delta\beta}{\beta} (-4p^2\beta^2), \quad (1)$$

where R_{pp} is the reflectivity for P-waves; p is the ray parameter; α , β , and ρ are,

respectively, the average P-wave velocity, S-wave velocity, and density of the upper and lower layers; $\Delta\alpha$, $\Delta\beta$, and $\Delta\rho$ are, respectively, the differences between the P-wave velocities, S-wave velocities, and densities in the upper and lower layers; and i is the average between the angle of P-wave incidence and P-wave transmission. In our implementation, the user specifies, as input to the modelling code, maps of P-wave reflectivity, $\frac{\Delta\alpha}{\alpha}$, S-wave reflectivity, $\frac{\Delta\beta}{\beta}$, and density reflectivity, $\frac{\Delta\rho}{\rho}$, as well as independent background P-wave velocity, α , and S-wave velocity, β , functions. We consider i to be the angle of incidence calculated from the ray parameter, p , by multiplication by the value of the background P-wave velocity function, α , just above the reflector.

One of the problems of using this implementation is that predicted Rpp values have a tendency to “blow-up” near the critical angle. This is related to the fact that the Zoeppritz equations and the associated Aki-Richards approximation describe the reflection and transmission of plane waves; equations describing reflection and transmission of spherical waves do not exhibit this behaviour, but are more complicated. Large reflection coefficients at very large incidence angles are especially problematic because they cause very oblique, high-angle, non-specular raypaths to have very large amplitudes. In order to reduce this behaviour, we implemented a method for modifying the reflection coefficients for incidence angles larger than the largest angle expected for Snell’s Law reflections. An input parameter to the modelling code is the maximum expected offset for reflections. If not specified, the offset is calculated as the maximum distance between any receiver position and the source position. During the modelling, the incidence angle for this offset, i_{\max} , is determined by ray tracing. If an incidence angle, i , is encountered that is larger than i_{\max} , we calculate $\Delta i = i - i_{\max}$. Then, instead of using the reflection coefficient calculated for that incidence angle, i , which may be undesirably large, the reflection coefficient that is used for that raypath is the one corresponding to an incidence angle of $i_{\max} - \Delta i$. In this way, the reflection coefficient values “wrap around” at the value of i_{\max} , back down to lower values. We are not concerned about post-critical reflection coefficients because our ray-tracing method fails for post-critical incidence and because we wish to model only normal sub-critical reflections. If critical incidence is encountered during the modelling but reflection coefficients are still needed for those offsets, the nearest non-critical raypath is used.

EXAMPLES

To illustrate the effect of introducing AVO in the modelling method and to check the accuracy of the implementation, 3D shot records were produced in a constant velocity setting over a single flat reflector with a constant reflection coefficient in x and y. Two shots were modelled; one in the middle of a square patch of receivers and one in the corner of the same patch. The lateral dimensions of the patch were 2775 m by 2775 m, with a receiver spacing of 15 m in x and y. The reflector was located at a depth of 1000 m and the P-wave velocity, S-wave velocity, and density of the medium between the surface and the reflector were 3000 m/s, 1500 m/s, and 2000 kg/m³, respectively. The wavelet used had a spectrum of [0 0 110 120] Hz. In the first case, the reflectivity function at the

reflector was a constant, 0.1. In the second case, AVO was introduced in the model by setting $\frac{\Delta\alpha}{\alpha}$ equal to 0.1, $\frac{\Delta\beta}{\beta}$ equal to 0.3, and $\frac{\Delta\rho}{\rho}$ equal to 0.1. These values give a reflection coefficient of 0.1 at zero offset, equal to that used in the case without AVO. Figure 3 shows the expected reflection amplitudes versus incidence angle for these parameters, calculated using the Zoeppritz equations and also the Aki-Richards approximation. The figure also shows the amplitude versus incidence angle function used in the modelling code, which we term Born-approximate Aki-Richards. The curves differ because of slight differences in the interpretation of the provided parameters. In the case of the Zoeppritz equations, the reflecting interface is considered to be between two homogeneous half-spaces. The specified values of 3000 m/s, 1500 m/s, and 2000 kg/m³ are considered to be the properties of the upper layer; those properties and the alpha-, beta-, and rho-reflectivities are used to compute the corresponding properties of the lower layer. In the conventional Aki-Richards approximation the same specified values of the three reflectivities are used in Equation 1, and the values of i , incidence angle, and β , S-wave velocity, are considered to be the average of those parameters in both the upper and lower layers. In contrast to this, the Born-approximate Aki-Richards model considers the values of i and β to be determined entirely by the background velocity functions, simply 3000 m/s for P-waves and 1500 m/s for S-waves in this constant velocity case. The choice of AVO model introduced in the modelling method was driven by ease of implementation; since the background velocities and reflectivities were already decoupled for the purpose of phase-shifting, a similar decoupling in the calculation of AVO effects seemed appropriate.

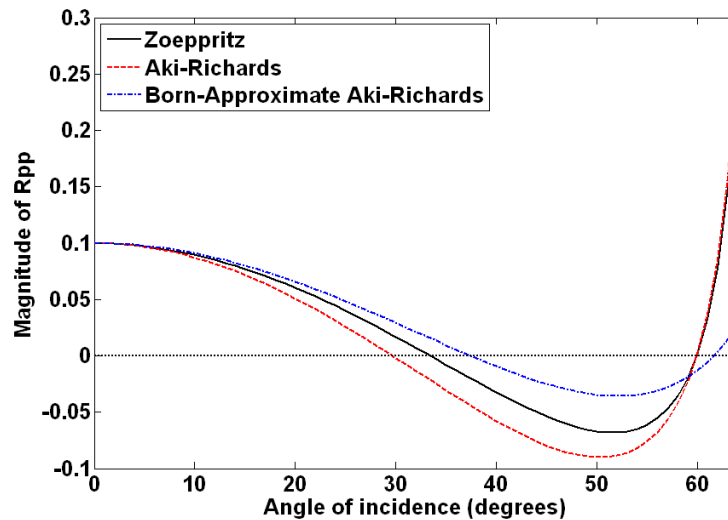


FIG. 3. AVO curves for constant velocity test model. The three curves are the exact Zoeppritz equations, the Aki-Richards approximation, and the AVO relationship implemented in our Rayleigh-Sommerfeld code, which is based on applying the first-order Born approximation to the Aki-Richards approximation.

Figure 4 shows vertical slices through the 3D shots for the no-AVO and AVO cases. As expected, in the case without AVO, amplitudes decay slightly with offset in

accordance with geometric spreading; since the reflections recorded at greater offsets correspond to longer total path lengths travelled, they experience more amplitude loss. In the case with AVO, the amplitudes are seen to decay faster and even switch polarity in the case of the corner shot. Figure 5 shows the extracted amplitudes from the reflections observed in Figure 4. To isolate the AVO effects, the amplitudes were corrected for geometric spreading using a simple multiplication by r , where r is the path length of the ray from source to reflector to receiver. The extracted amplitudes have also been normalized to a value of 0.1 at zero offset for comparison with the model curves. As expected, the no-AVO shot shows constant amplitudes with offset, whereas the amplitudes from the AVO shot show a distinct change with offset. Since the background velocity is constant, offset and incidence angle are related simply by $\tan i = \frac{x}{2z}$.

This allowed the Born-approximate Aki-Richards model curve from Figure 3 to be converted into a function of offset, for direct comparison to the extracted amplitudes in Figure 5. The extracted amplitudes from both the AVO shots show very similar decay shapes compared to the model values. The similarities between the theoretical case and the observed results indicate that the implementation is successfully introducing realistic AVO effects and can be applied with confidence in more complex settings.

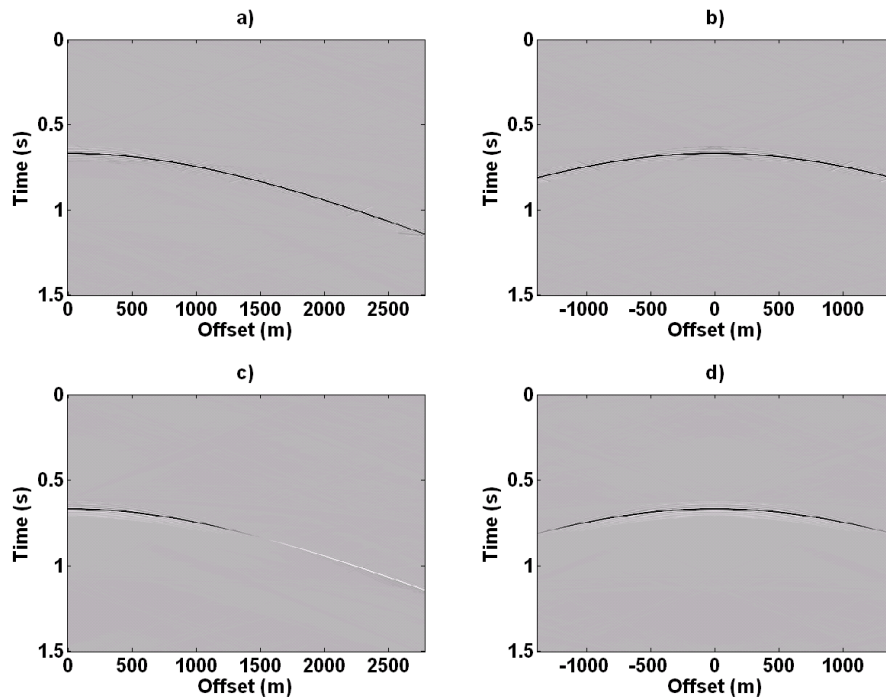


FIG. 4. Constant x slices through the shot location from 3D shot records produced in a constant velocity medium. a) Shot located in the corner of the receiver patch, with no AVO; b) Shot located in the centre of the receiver patch, with no AVO; c) Shot located in the corner of the receiver patch, with AVO; d) Shot located in the centre of the receiver patch, with AVO.

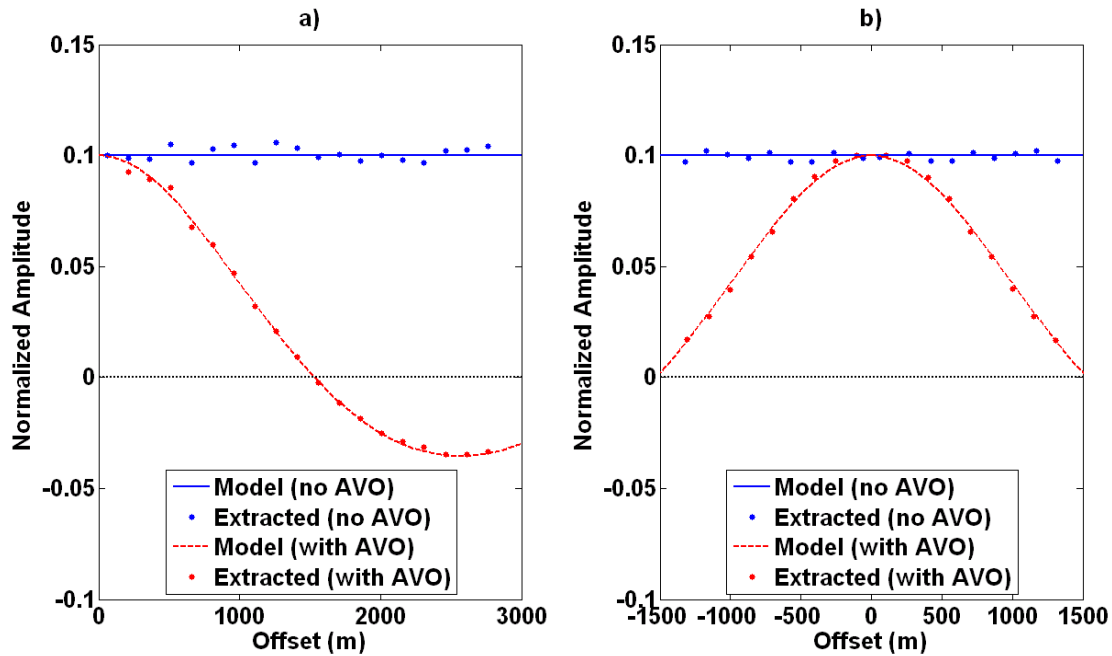


FIG. 5. Extracted amplitudes from the reflections displayed in Figure 4 for a) the corner shot and b) the centre shot, corrected for geometrical spreading and normalized to a value of 0.1 at zero offset. Extracted amplitudes show a strong correlation to the model curves (constant in the no-AVO case and equal to the Born-approximate Aki-Richards model in the AVO case).

Ray tracing in these shots accounted for less than 1 % of the total time for the modelling. Compared to the shots without AVO, the shots with AVO took between 5 and 10 % longer to model. In our previous paper (Margrave and Cooper, 2007) we demonstrated that Kirchhoff modelling was significantly slower than Rayleigh-Sommerfeld modelling, showing run-times of 600-6000 % longer. Though obviously not an exhaustive test, the above example demonstrates that the small slowdown that we observe in order to incorporate AVO in the Rayleigh-Sommerfeld method does not change the large efficiency advantage of Rayleigh-Sommerfeld compared to Kirchhoff.

APPLICATION

Our main purpose in improving the Rayleigh-Sommerfeld modelling method was to use it to create a new version of the channel model described by Margrave and Cooper (2007). The new model was designed to be more geologically complex and larger. As part of the improved geological complexity, AVO effects were desired. Margrave et al. (2008) describe the process by which the new model was created and show in detail the resulting velocity and density distributions. Here we show the results from applying the AVO-inclusive Rayleigh-Sommerfeld method to this new model.

As discussed previously, though the Rayleigh-Sommerfeld method can model reflectivities that are laterally varying, its current implementation does not properly handle laterally varying propagation velocities. As a result, the modelled seismic data shown here, produced with the Rayleigh-Sommerfeld method over the new model only included a single channel layer, not the entire stack described by Margrave et al. (2008).

The P- and S-wave velocities and the densities of the target layer were converted to the required $\frac{\Delta\alpha}{\alpha}$, $\frac{\Delta\beta}{\beta}$, and $\frac{\Delta\rho}{\rho}$, as shown in Figure 6 a), b), and c). The background P-wave velocity profile required for the propagation of the wavefield is shown in Figure 6 d), along with the S-wave velocity and density functions. Based on these properties, Figure 7 shows the theoretical AVO profile for two points on the reflector, one in the regional facies and another in one of the target sands; the locations of these two points are indicated on the maps in Figure 6.

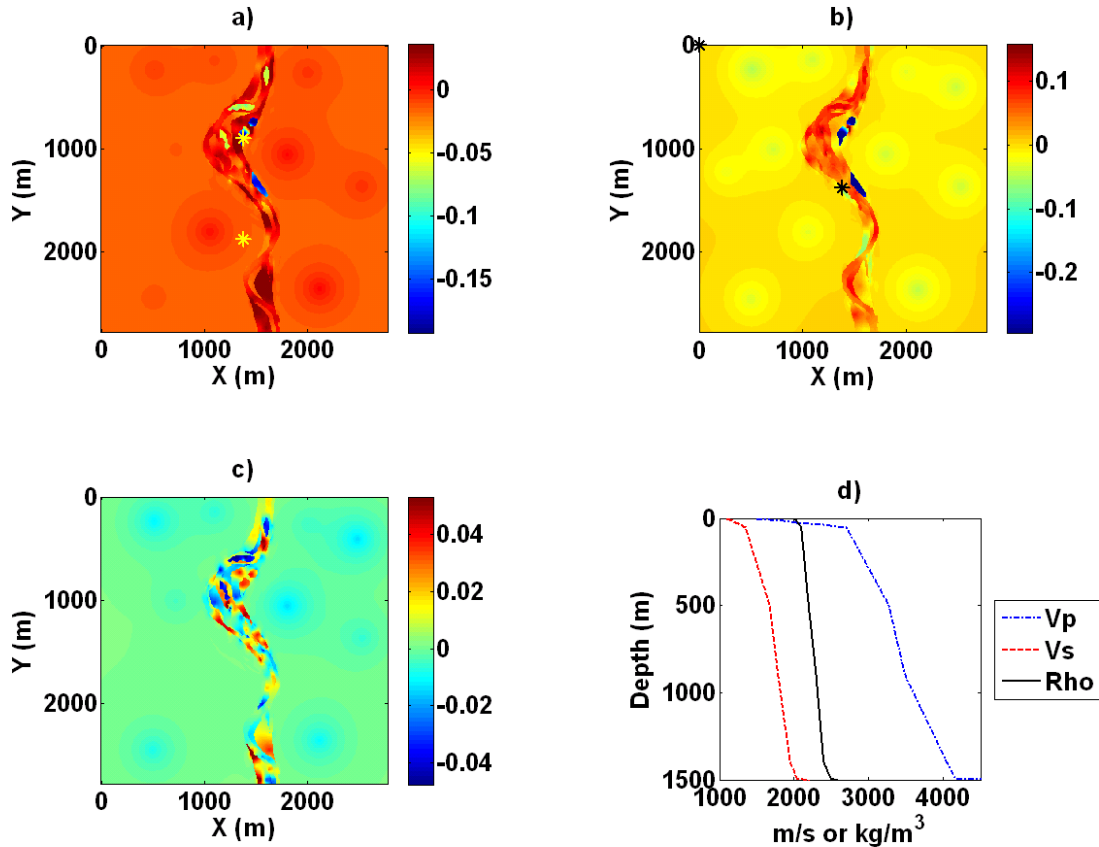


FIG. 6. a) P-wave reflectivity map of the target layer; b) S-wave reflectivity map; c) Density reflectivity map; d) Background P-wave velocity, S-wave velocity, and density profiles as a function of depth. The locations of the two points whose AVO curves are shown in Figure 7 are indicated by yellow stars on the map in a) at $x=1380$ m, $y=900$ m and $x=1380$ m, $y=1875$ m. The locations of the two shots displayed in Figures 8-12 are indicated by black stars on the map in b) at $x=0$ m, $y=0$ m and $x=1380$ m, $y=1380$ m.

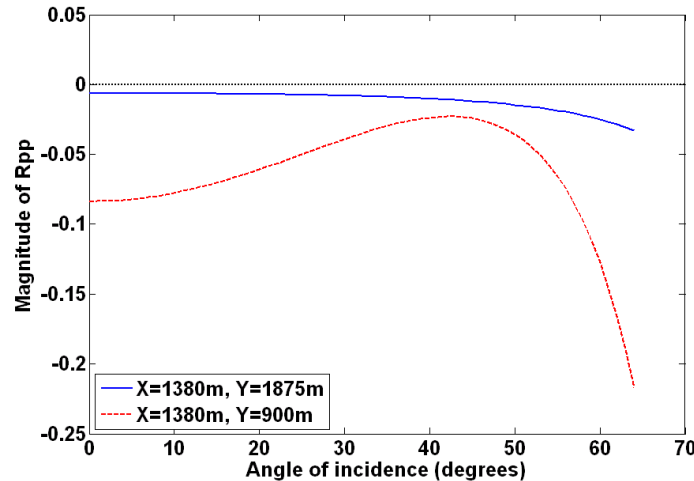


FIG. 7. Model AVO curves for a point in the regional facies of the model (blue solid line) and for a point in a channel sand body (red dashed line), calculated from the properties shown in Figure 6.

To simulate a larger seismic survey compared to the previous channel model, the Margrave et al. (2008) model was scaled to a horizontal extent of 2775 m by 2775 m, with the target channel reflector at a depth of 1000 m. A second, featureless reflector, with a constant reflection coefficient of 0.1 and no AVO effects, was placed at a depth of 500 m. The reflectivity was defined on a grid of 7.5 m, which allowed for source and receiver spacings of 15 m. For all shots, receivers were located every 15m in x and y over the whole 2775 m by 2775 m area. This spacing, coupled with the overburden velocity profile allowed for the use of frequencies up to 120 Hz, without encountering spatial aliasing of reflections. The modelled data was sampled in time at 0.004 s, with a record length of 1.5 s. Figures 8 and 9 c) and d) show a shot from the edge of the model (at $x=0$ m, $y=0$ m) and a shot from the middle of the model (at $x=1380$ m, $y=1380$ m). For comparison, Figures 8 and 9 a) and b) show the same shots, without AVO effects at the channel level. The difference between Figure 8 and Figure 9 is that Figure 8 shows constant y slices, at y equal to the y coordinate of the shot, and Figure 9 shows constant x slices, at x equal to the x coordinate of the shot. As expected, the amplitudes of the no-AVO events show simply amplitude decay with offset, in accordance with geometrical spreading losses corresponding to the longer path lengths. Complicated diffraction effects are also observed associated with the channel. Comparing the no-AVO shots to the shots including AVO effects, there are significant differences occurring at large offsets, with higher amplitudes associated with channel diffractions occurring when AVO effects are included. Figure 7 is in agreement with this observation, since the reflection coefficient magnitudes increase greatly at large angles of incidence when AVO effects in the channel are encountered. Figure 10 shows time slices through the same shots shown in Figures 8 and 9. Again, differences at long offsets are evident, especially in the corner shot. Figure 11 shows the f-k spectra for the slices through the shots shown in Figure 8 c) and d). The spectra do not show evidence of spatial aliasing, supporting the choices of grid spacing and maximum frequency used in the modelling.

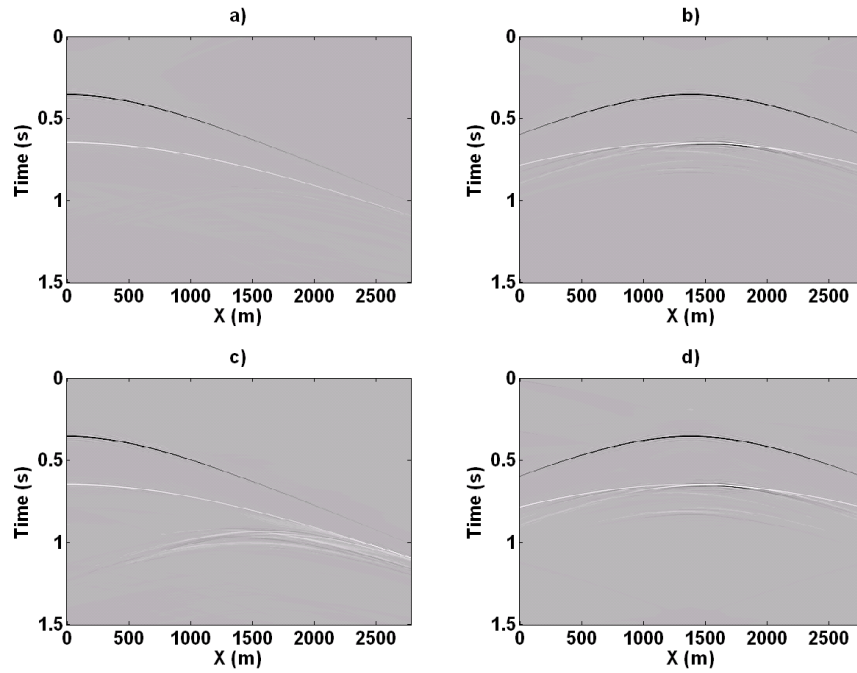


FIG. 8. Constant y slices at $y=y_{\text{shot}}$ for a) Corner shot without AVO ($y=0$ m), b) Centre shot without AVO ($y=1380$ m), c) Corner shot with AVO ($y=0$ m), and d) Centre shot with AVO ($y=1380$ m). Amplitudes of the slices in a) and b) are scaled relative to the slices in c) and d).

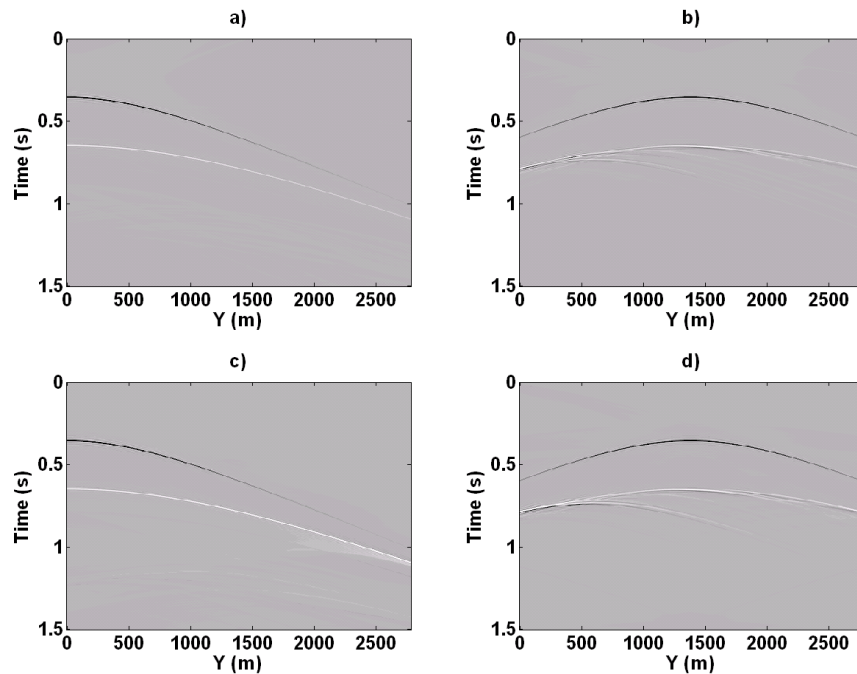


FIG. 9. Constant x slices at $x=x_{\text{shot}}$ for a) Corner shot without AVO ($x=0$ m), b) Centre shot without AVO ($x=1380$ m), c) Corner shot with AVO ($x=0$ m), and d) Centre shot with AVO ($x=1380$ m). Amplitudes of the slices in a) and b) are scaled relative to the slices in c) and d).

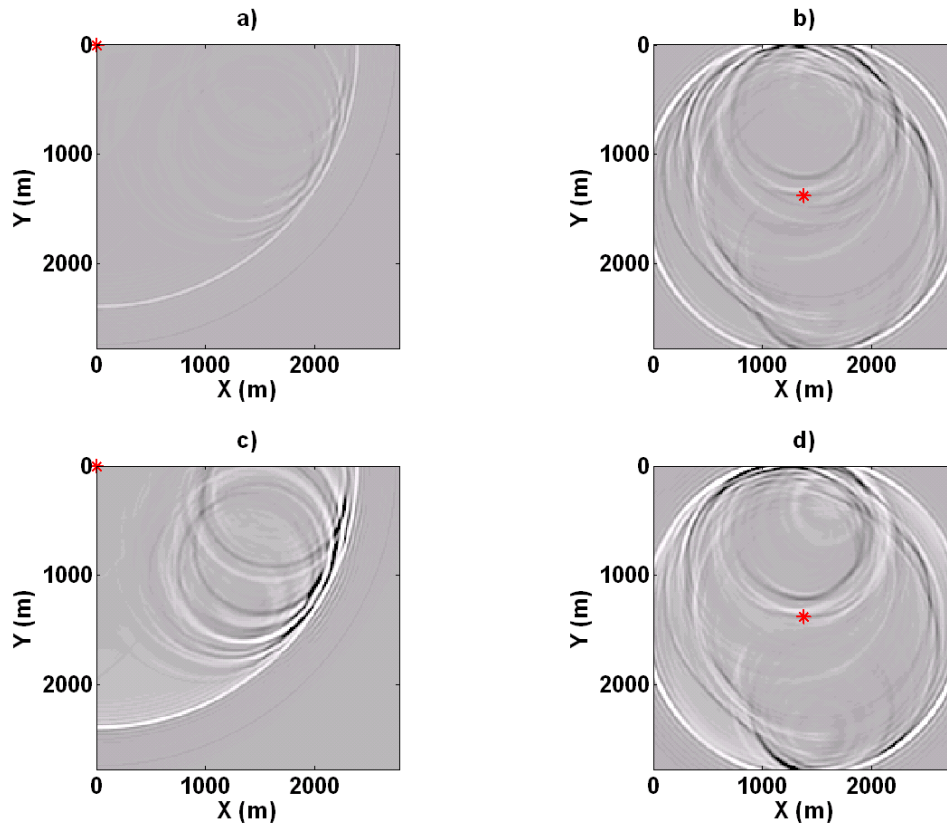


FIG. 10. Constant time slices for a) Corner shot without AVO ($t=1$ s), b) Centre shot without AVO ($t=0.8$ s), c) Corner shot with AVO ($t=1$ s), and d) Centre shot with AVO ($t=0.8$ s). Amplitudes of the slices in a) and b) are scaled relative to the slices in c) and d). Shot locations are indicated by red stars.

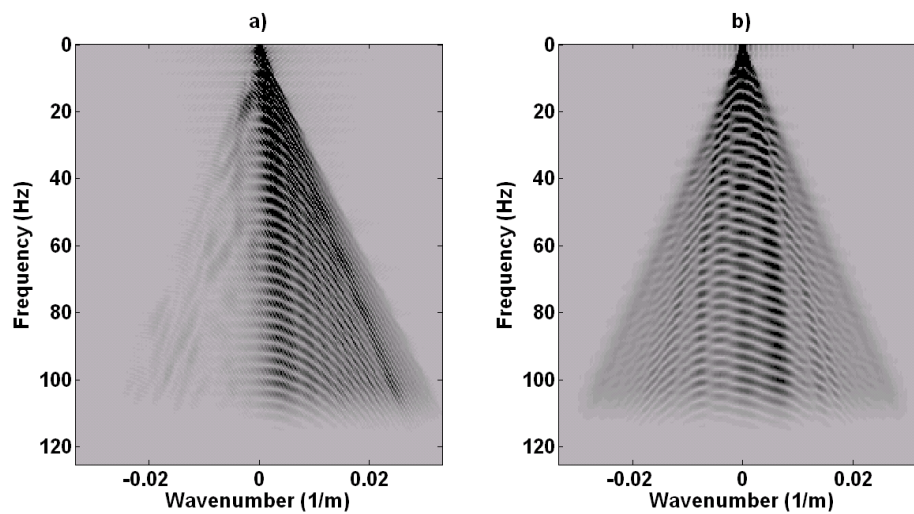


FIG. 11. a) f-k amplitude spectrum for shot slice shown in Figure 8 c). b) Spectrum for shot slice shown in Figure 8 d). The spectra do not show evidence of spatial aliasing over the modelled frequency band.

The four shots displayed in Figures 8 through 10 were migrated using a prestack Kirchhoff migration algorithm, described by Cooper et al. (2007). Depth slices at the channel level from the resulting migrations are shown in Figure 12. The four shots image the channel well, though there are differences especially at long offsets, where larger amplitudes are observed from the AVO effects of the channel. The increased variability in the off-channel amplitudes in the AVO case results from the effect of the S-wave reflectivity (Figure 6 b), which is not incorporated into the case without AVO.

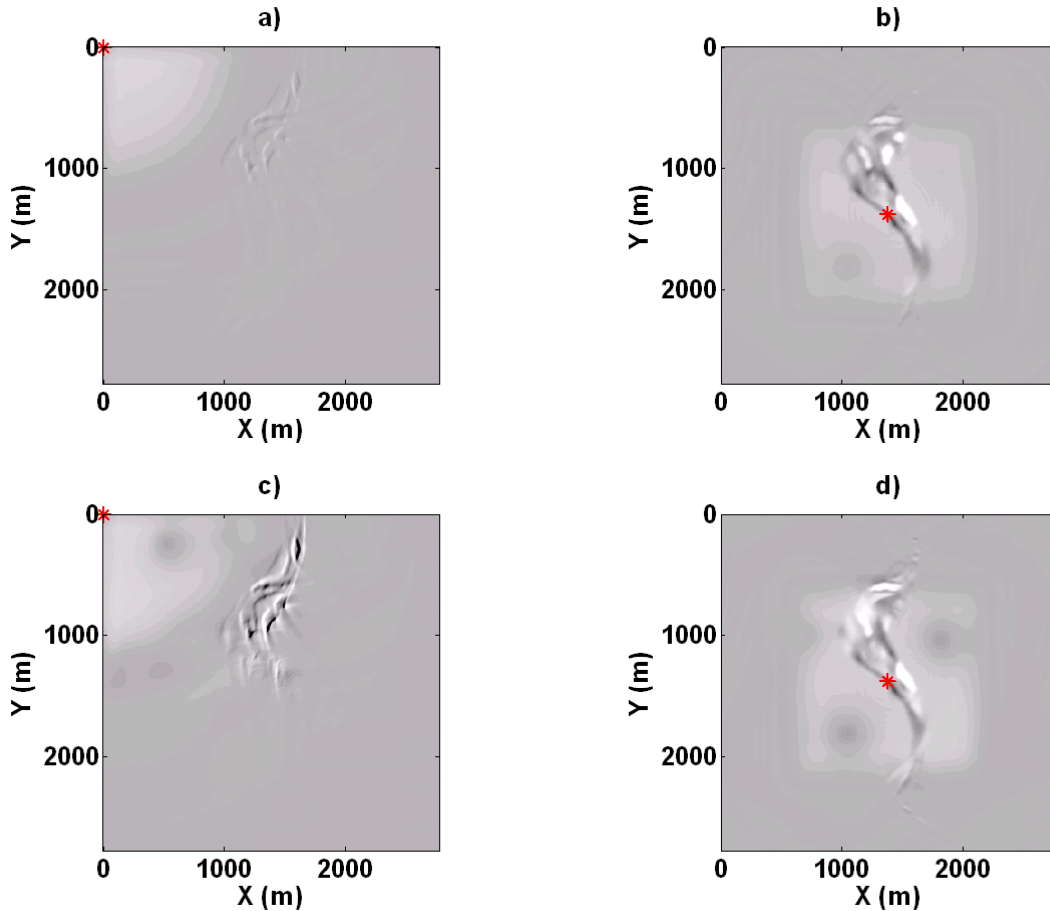


FIG. 12. Depth slices at the channel level (1000 m) from prestack Kirchhoff migrations of the four shots displayed in Figures 8-10. a) Corner shot without AVO; b) Centre shot without AVO; c) Corner shot with AVO; d) Centre shot with AVO. Amplitudes of the slices in a) and b) are scaled relative to the slices in c) and d). Shot locations are indicated by red stars.

Currently, shots corresponding to all of the 137641 possible source locations on a 15 m by 15 m grid are being modelled and migrated in MATLAB. A subset of those shots occurring along a shotline at $x=1380$ m was used to produce two migrated common-image gathers (Figure 13), for the regional reflection point and the reflection point in the channel sand, whose locations were shown in Figure 6. The two reflectors, the featureless reflector at 500 m depth and the channel reflector at 1000 m, are clearly visible. The common-image gathers show slight deviations from horizontality at large source-image point offsets, but show generally good images for offsets smaller than the depth of each

reflector. The extracted amplitudes at the channel level (Figure 14) show a similar change in amplitude with offset compared to the theoretical curves from Figure 7, though the extracted amplitudes decay faster than the model curves, especially for the image point in the channel sand. It is unclear at this stage whether this is a deficiency in properly handling amplitudes in the migration algorithm, or a complexity produced by the modelling method that did not exhibit itself during the constant velocity test, such as a mixing of AVO effects from adjacent image points. If the second case were true, it may be either an inadequacy of the modelling method or a real consequence of attempting to observe AVO signatures from small bodies. The theory of Zoeppritz reflection coefficients assumes plane waves incident on a featureless reflector, both of which are infinite in spatial extent. Clearly this is not the case here. Despite this uncertainty, the extracted amplitudes do show that a significant AVO effect was produced in the migrated data from the channel model, with definite observable differences between modelled lithologies.

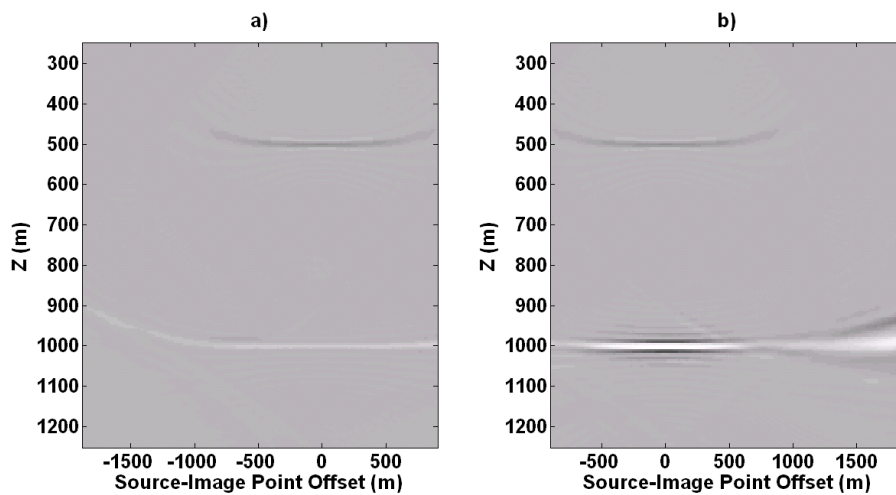


FIG. 13. Common-image gathers for a) an image point in the regional facies (at $x=1380$ m, $y=1875$ m) and b) an image point in the channel sand (at $x=1380$ m, $y=900$ m), produced by migrating 186 shots along the shotline at $x=1380$ m. The locations of the image points are shown in Figure 6. The amplitudes in a) were scaled relative to the amplitudes in b).

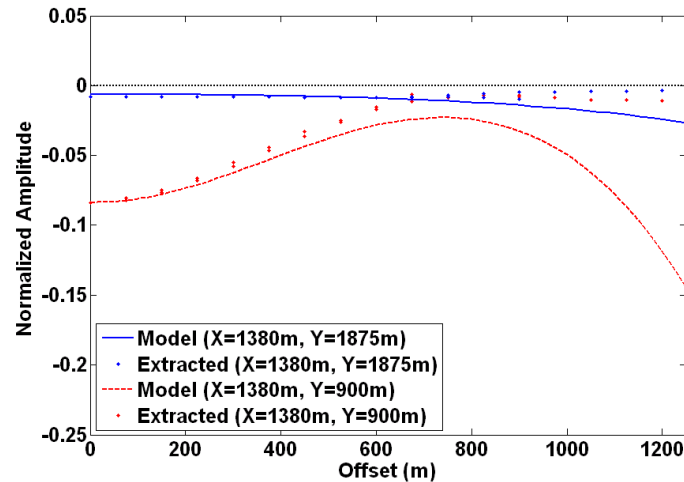


FIG. 14. Extracted amplitudes from the common-image gathers shown in Figure 13, compared to the model AVO curves from Figure 7 converted from angle to offset based on ray tracing. Extracted amplitudes were normalized such that the zero-offset amplitude of the channel sand image point matched the model.

DISCUSSION AND CONCLUSIONS

Adding the ability to include angle-dependent reflection coefficients in the Rayleigh-Sommerfeld method allows us to model more realistic stratigraphic effects, compared to the previous implementation. In order to include AVO, ray tracing is used, which adds to the total computation time; still Rayleigh-Sommerfeld is very efficient compared to Kirchhoff modelling and can produce a high-frequency response that would be challenging for a finite-difference method. The way in which AVO is implemented in the method has some limitations; by using a variant of the Aki-Richards approximation we are assuming locally planar wavefronts whose incidence angles can be described by ray tracing. A further extension of the Rayleigh-Sommerfeld method using Gabor transforms would accommodate laterally varying background propagation velocities; this would allow the full channel stack of Margrave et al. (2008) to be modelled. In addition to implementing this extension, future work will involve completing the modelling of all shots from the channel model described above, and trying to better understand the complexities of the results, especially the post-migration amplitudes.

ACKNOWLEDGEMENTS

We gratefully acknowledge financial support provided by the sponsors of CREWES, the sponsors of POTSI, NSERC, Alberta Ingenuity, and MITACS.

REFERENCES

- Aki, K. and P. G. Richards, 2002, *Quantitative Seismology*, Second Edition: University Science Books.
- Berkhout, A. J., 1993, A unified approach to acoustical reflection imaging. I: The forward model: *Journal of the Acoustical Society of America*, **93**, 2005-2016.
- Cooper, J. K., G. F. Margrave, and D. C. Lawton, 2007, Simulations of seismic acquisition footprint: *CREWES Research Report*, **19**, 28.1-28.20.
- Ersoy, O. K., 2007, *Diffraction, Fourier optics, and imaging*: Wiley InterScience.
- Gazdag, J., 1981, Modeling of the acoustic wave equation with transform methods: *Geophysics*, **46**, 854-859.

Margrave, G. F. and J. K. Cooper, 2007, Seismic modelling in 3D for migration testing: CREWES Research Report, **19**, 23.1-23.24.

Margrave, G. F., S. Taylor, and J. K. Cooper, 2008, Towards realistic 3D elastic models of Canadian channel and reef structures: CREWES Research Report, this volume.